Nucleon, Δ, and Ω excited state spectra in $N_f = 2 + 1$ lattice QCD

J. Bulava,[1] R. G. Edwards,[2] E. Engelson,[3] B. Joó,[2] H-W. Lin,[4] C. Morningstar,[5] D. G. Richards,[2] and S. J. Wallace[3]

(Hadron Spectrum Collaboration)

[1]*NIC, DESY, Platanenallee 6, D-15738, Zeuthen, Germany*
[2]*Thomas Jefferson National Accelerator Facility, Newport News, Virginia 23606, USA*
[3]*Department of Physics, University of Maryland, College Park, Maryland 20742, USA*
[4]*Department of Physics, University of Washington, Seattle, Washington 98195-1560, USA*
[5]*Department of Physics, Carnegie Mellon University, Pittsburgh, Pennsylvania 15213, USA*

The energies of the excited states of the nucleon, Δ, and Ω are computed in lattice QCD, using two light quarks and one strange quark on anisotropic lattices. The calculation is performed at three values of the light quark mass, corresponding to pion masses $m_\pi = 392(4)$, 438(3), and 521(3) MeV. We employ the variational method with a large basis of interpolating operators enabling six energies in each irreducible representation of the lattice to be distinguished clearly. We compare our calculation with the low-lying experimental spectrum, with which we find reasonable agreement in the pattern of states. The need to include operators that couple to the expected multihadron states in the spectrum is clearly identified.

PACS numbers: 12.38.Gc, 11.15.Ha, 12.38.Lg

I. INTRODUCTION

The theoretical determination of the spectrum of baryon resonances from the fundamental quark and gluon degrees of freedom is an important goal for lattice QCD. Recently a number of groups have performed lattice computations for $N_f = 2 + 1$ QCD with two light-quark flavors (up and down) and one more massive quark flavor (strange) [1–8]. Different actions have been used and several analyses achieve a pion mass close to the physical limit. A recent analysis used a reweighting technique to perform calculations at the physical pion mass [9]. One focus of attention has been the determination of the lowest baryon mass for each isospin and strangeness. Good agreement has been achieved between different calculations. The experimental masses are reproduced typically with discrepancies ranging from 1% to 8%.

Another focus of attention is the excited state spectrum of baryons. Recent works have progressed beyond quenched QCD [10,11], which omits the effects of light quarks from the gauge ensembles. Two light-quark flavors ($N_f = 2$) were used in Ref. [12]. In this work we use ensembles of gauge configurations developed in Ref. [1] for $N_f = 2 + 1$ QCD with dynamical light and strange quarks.

There are ongoing experimental programs aimed at determining the spectra and properties of excited baryons at the Thomas Jefferson National Accelerator Facility. Reference [13] provides an overview of some recent experimental results.

Excited baryon states can be quite massive, and a small lattice spacing in the time direction is best for observing their signals, which decrease exponentially with time. If the same lattice spacing were used in spatial and time directions the computational cost would be unnecessarily high. The Hadron Spectrum Collaboration has undertaken a program to solve QCD using anisotropic lattices that have a smaller spacing, a_t, in the time direction. In this work we use $16^3 \times 128$ lattices with a renormalized anisotropy $\xi = 3.5$ [14], i.e., $a_t = a_s/3.5$, where a_s is the spatial lattice spacing. A Symanzik-improved gauge and a clover-improved Wilson fermion action have been used to generate gauge ensembles for $N_f = 2 + 1$ QCD. [1] The three ensembles used in this work have pion masses of 392(4) MeV, 438(3) MeV, and 521(3) MeV. The effects of charm, bottom and top quarks are neglected because the baryons under study have only light quarks in their valence structures and the loop contributions of the neglected quarks are suppressed by their large masses.

For families of particles with given isospin and strangeness, spectra are calculated in the six double-valued irreducible representations (irreps) of the octahedral group. There are three irreps for even parity that are labeled with a g subscript (*gerade*) and three for odd-parity that are labeled with a u subscript (*ungerade*). They are: G_{1g}, H_g, G_{2g}, G_{1u}, H_u, and G_{2u}. Operators that transform according to one of these irreps do not mix with those of other irreps because of the octahedral symmetry.

A large basis of interpolating field operators is needed in order to extract the spectrum of excited states. We have developed many such operators for each isospin, strangeness and octahedral irrep in previous works [15]. In this work we select sets of 7 to 11 operators in each irrep. Continuum values of total angular momenta show up in lattice simulations as patterns of degenerate energies in the continuum limit that match the patterns in Table I for the

TABLE I. The number of occurrences of double-valued irrep Λ of the octahedral group for half-integer values of continuum spin J. N is the dimension of the irrep.

Λ	N	J	1/2	3/2	5/2	7/2	9/2	11/2
G_1	2		1	0	0	1	1	1
H	4		0	1	1	1	2	2
G_2	2		0	0	1	1	0	1

subduction of spin J to the double-valued irreps of the octahedral group.

For example, a state in one of the G_2 irreps is a signal for the subduction of continuum spin $\frac{5}{2}$ or higher. Because spin $\frac{5}{2}$ has six magnetic substates and the lattice G_2 irrep has dimension two, there must be four degenerate partner states from the four-dimensional H irrep in order to realize the six linearly independent states that are required. For spin $\frac{7}{2}$, there must be degenerate partner states in the G_1, H and G_2 irreps in order to realize the total of eight magnetic substates.

This paper is organized as follows. In Sec. II, we review the lattices used and the basic features of the action and quark masses, the baryon operators, the smearing of quark fields based on eigenvectors of the gauge-covariant lattice Laplacian, the pruning of operators to obtain suitable sets for calculations of matrices of correlation functions and the variational method with eigenvectors fixed at one time value. As we have shown in previous work [12], smearing of the source and sink operators is important for calculations of baryon spectra because it reduces contributions from short wavelength fluctuations. We use the recently developed distillation method of Ref. [16] in which source and sink quark operators are smeared by applying eigenvectors of the gauge-covariant Laplacian, $-\nabla^2$.

The orthogonality of the eigenvectors produces a factorization of the problem. One part consists of the smeared baryon operators based on N_{eig} eigenvectors of the scalar Laplacian $-\nabla^2$ on each time slice for each quark. The other consists of correlation functions corresponding to the parallel transport of smeared quark operators formed from the eigenvectors of the Laplacian from the source time slice to the sink time slice. These elementary quark correlation functions are called "perambulators" for short. They are universal in the sense that they may be used for any baryon or meson operators. The distillation method provides an "all-to-all" calculation in the sense that propagators are calculated from all N_{eig} eigenvectors of $-\nabla^2$ at the source to all N_{eig} eigenvectors at the sink.

In Sec. III we report calculations for the nucleon and show details of the fits to obtain energies and the results for the spectrum at the lowest pion mass, 392 MeV. In Sec. IV we report summary results for the nucleon, Δ and Ω spectra for all three pion masses and comparisons with experimental resonances. The Ω spectrum of low-lying excited states is interesting because little experimental information is available. It also helps to set the overall scale for baryon spectra, for which we use the ground state Ω baryon mass at each value of m_π.

Section V gives a summary of the results.

II. LATTICES, OPERATORS, AND MATRICES OF CORRELATION FUNCTIONS

References [1,14] presented the tuning of quark masses and other parameters for $N_f = 2 + 1$ QCD on the anisotropic $16^3 \times 128$ lattice used in this work. Reference [16] presented the method of smearing hadronic operators using an expansion in terms of eigenvectors of the three-dimensional lattice Laplacian. Because those references provide the foundation for the present work, we summarize their findings in this section.

Table II shows the three sets of quark masses from Ref. [1] used in this work together with values for the pion mass, the kaon mass and the Ω baryon mass. The value of the pion mass in MeV units is obtained by using the Ω mass at each point to set the scale. We also show the number of gauge configurations used. For each configuration we compute correlation functions from four different time sources and average them in order to take account of correlations.

Baryon operators used in this work were developed in Ref. [15]. For the baryons that we have considered, the single-site (SS) forms of the operators are given in Table III. Most operators incorporate gauge-covariant displacements of the quarks relative to one another in order to obtain nontrivial shapes. The displaced operators are projected to irreps of the octahedral group by summing over all lattice rotations applied to the shapes and spins with coefficients that project out the irrep operators. Many operators are so obtained and in the final step they are "pruned" to sets of between 7 and 11 operators for each N and Δ irrep. For Ω, we use the same operators as for Δ

TABLE II. Lattice parameters. Three sets of values (in temporal lattice units) of the light-quark mass, m_ℓ, the strange-quark mass, m_s and the resulting π meson, K meson and Ω-baryon masses. The corresponding values of m_π in MeV are given in the last row based on using Eq. (15).

ensemble	1	2	3
m_ℓ	-0.0840	-0.0830	-0.0808
m_s	-0.0743	-0.0743	-0.0743
Volume	$16^3 \times 128$	$16^3 \times 128$	$16^3 \times 128$
N_{cfgs}	344	570	481
t_{sources}	4	4	4
m_π	0.0691(6)	0.0797(6)	0.0996(6)
m_K	0.0970(5)	0.1032(5)	0.1149(6)
m_Ω	0.2951(22)	0.3040(8)	0.3200(7)
m_π (MeV)	392(4)	438(3)	521(3)

TABLE III. Baryons and the corresponding three-quark elemental operators. Columns 1 to 4 show the symbol, isospin, strangeness, and the form of elemental single-site operators used. The last three columns show the numbers of embeddings of single-site operators with irreps G_{1g}, G_{2g}, and H_g, respectively.

	I	S	$B_{\alpha\beta\gamma}$	G_{1g}	G_{2g}	H_g
N	$1/2$	0	$(u_\alpha d_\beta - d_\alpha u_\beta)u_\gamma/\sqrt{2}$	3	0	1
Δ	$3/2$	0	$(u_\alpha u_\beta d_\gamma + u_\alpha d_\beta u_\gamma + d_\alpha u_\beta u_\gamma)/\sqrt{3}$	1	0	2
Ω	0	-3	$(s_\alpha s_\beta s_\gamma + s_\alpha s_\beta s_\gamma + s_\alpha s_\beta u_\gamma)/\sqrt{3}$	1	0	2

except that the number is limited to 6 in each irrep. The operators are selected to have good signal to noise characteristics and correlation matrices with low condition numbers at a time close to the source. Low condition number (ratio of largest to smallest eigenvalue) is a proxy for linear independence, which follows because two linearly dependent operators would give a zero eigenvalue for a matrix of correlation functions and an infinite condition number. A full listing of operators is available upon request.

Table IV indicates the number and type of pruned operators for each irrep for N, Δ, and Ω baryons used in this work following the conventions of Ref. [15]. The types of operators are: SS (single-site); SD (singly displaced) with one quark gauge-covariantly displaced from the other two; DDI (doubly-displaced-I) with two quarks displaced in opposite directions from the third; and TDT (triply-displaced-T) with all quarks displaced to create a T shape.

In order to reduce couplings to short-wavelength lattice fluctuations, smearing of the operators is performed as in

TABLE IV. Numbers of operators of each type used in this work for N, Δ, and Ω matrices are listed for each irrep. SS denotes single-site (local) operators, SD denotes singly-displaced operators, DDI denotes doubly-displaced-I operators, DDL denotes doubly-displaced-L operators, and TDT denotes triply-displaced-T operators. Gauge-covariant displacements are used.

Baryon	Operator type	G_{1g}	G_{1u}	H_g	H_u	G_{2g}	G_{2u}
N	SS	2	1	1	1	0	0
N	SD	1	1	2	1	1	2
N	DDI	0	2	1	3	3	2
N	DDL	2	2	4	3	3	2
N	TDT	2	4	3	1	4	2
N	total	7	10	11	9	11	8
Δ	SS	0	0	1	2	0	0
Δ	SD	3	3	2	0	4	2
Δ	DDI	2	2	1	2	0	0
Δ	DDL	3	3	2	2	4	4
Δ	TDT	2	1	3	4	3	3
Δ	total	10	9	9	10	11	9
Ω	SS	0	0	1	2	0	0
Ω	SD	3	3	2	0	4	2
Ω	DDI	2	2	1	2	0	0
Ω	DDL	1	1	2	2	2	4
Ω	total	6	6	6	6	6	6

Ref. [16]. The method is called "distillation" and it uses the eigenvectors of the gauge-covariant, three-dimensional Laplacian operator. The kth eigenvector depends on a color index, a, and the spatial coordinates, $\mathbf{x}$ and is written as $v_{a\mathbf{x}}^{(k)}$. It obeys the eigenvalue equation

$$(-\nabla^2)_{\mathbf{xy}}^{ab} v_{b,\mathbf{y}}^{(k)} = \lambda_k v_{a\mathbf{x}}^{(k)}, \tag{1}$$

where a and b are color labels. Ordering is imposed such that increasing k corresponds to increasing eigenvalues λ_k.

A sum over all $M = N_c \times N_x \times N_y \times N_z$ eigenvectors for a given lattice provides a decomposition of unity on time slice t, i.e.,

$$\sum_{k=1}^{M} v_{a,\mathbf{x}}^{(k)}(t) v_{b,\mathbf{y}}^{(k)\dagger}(t) = \delta^{ab}\delta_{\mathbf{xy}}. \tag{2}$$

A sum over only the N_{eig} lowest eigenvalues provides the distillation operator on time slice t as the following projection,

$$\Box_{\mathbf{xy}}^{ab}(t) = \sum_{k=1}^{N_{\mathrm{eig}}} v_{a,\mathbf{x}}^{(k)}(t) v_{b,\mathbf{y}}^{(k)\dagger}(t). \tag{3}$$

Applying the projection to a quark field yields

$$\Box_{\mathbf{xy}}^{ab}(t) q_\alpha^b(\mathbf{y}, t) = \sum_{k=1}^{N_{\mathrm{eig}}} v_{a,\mathbf{x}}^{(k)}(t) \tilde{q}_\alpha^{(k)}(t), \tag{4}$$

where the smeared field operator is defined by

$$\tilde{q}_\alpha^{(k)}(t) = v_{b,\mathbf{y}}^{(k)\dagger}(t) q_\alpha^b(\mathbf{y}, t). \tag{5}$$

The smeared field operator involves a sum over repeated indices b for color and $\mathbf{y}$ for space. It depends only on the Dirac index α, the Laplacian eigenvector label k, and time t. It is of rank $N_{\mathrm{eig}} \times N_\sigma$ vector on each time slice, where N_σ is the number of spinor components, i.e., four. A similar projection is used for displaced operators as discussed in Ref. [16].

Matrices of correlation functions are calculated as follows,

$$C_{ij}(t, t') = \sum_{\mathbf{xy}} \langle B_i(\mathbf{x}, t) B_j^\dagger(\mathbf{y}, t') \rangle, \tag{6}$$

where, using single-site operators,

$$B_i(\mathbf{x}, t) = C_i^{\alpha\beta\gamma}\epsilon^{abc}q_\alpha^{af_1}(\mathbf{x}, t)q_\beta^{bf_2}(\mathbf{x}, t)q_\gamma^{cf_3}(\mathbf{x}, t). \quad (7)$$

Superscripts a, b, and c are color indices while f_1, f_2, and f_3 are quark flavor indices. Constants $C_i^{\alpha\beta\gamma}$ weight the various Dirac components as required to form an irrep of the octahedral group. When each quark field is projected to the space of the N_{eig} lowest eigenvalues of the covariant Laplacian as in Eq. (4), the correlation function becomes (with sums over repeated indices understood)

$$C_{ij}(t, t') = \Phi_{i,k\ell m}^{\alpha\beta\gamma}(t)$$
$$\times \langle \tilde{q}_\alpha^{(k)}(t)\tilde{q}_\beta^{(\ell)}(t)\tilde{q}_\gamma^{(m)}(t)\bar{\tilde{q}}_{\bar{\alpha}}^{(\bar{k})}(t')\bar{\tilde{q}}_{\bar{\beta}}^{(\bar{\ell})}(t')\bar{\tilde{q}}_{\bar{\gamma}}^{(\bar{m})}(t')\rangle$$
$$\times \Phi_{j,\bar{k}\bar{\ell}\bar{m}}^{\bar{\alpha}\bar{\beta}\bar{\gamma}\,\dagger}(t') \quad (8)$$

where

$$\Phi_{i,k\ell m}^{\alpha\beta\gamma}(t) = C_i^{\alpha\beta\gamma}\sum_{\mathbf{x}}\epsilon^{abc}v_{a,\mathbf{x}}^{(k)}(t)v_{b,\mathbf{x}}^{(\ell)}(t)v_{c,\mathbf{x}}^{(m)}(t). \quad (9)$$

Further reduction of the correlation functions involves contractions of smeared quark fields that have the same quark flavor. That is different for each baryon but involves the same set of contractions as for unsmeared fields. With the smearing used here, each nonvanishing contraction yields a "perambulator" in the terminology of Ref. [16], i.e.,

$$\tau_{\alpha\bar{\alpha}}^{k\bar{k}}(t, t') = \langle \tilde{q}_\alpha^{(k)}(t)\bar{\tilde{q}}_{\bar{\alpha}}^{(\bar{k})}(t')\rangle_A$$
$$= v_{b,\mathbf{y}}^{(k)\dagger}(t)(M^{-1})_{\mathbf{yz},\alpha\bar{\alpha}}^{bc}(t, t')v_{c,\mathbf{z}}^{(\bar{k})}(t'), \quad (10)$$

where M is the Dirac matrix and $\langle\cdots\rangle_A$ denotes evaluation with a single gauge configuration. The perambulators are matrices in $N_{\mathrm{eig}} \times N_\sigma$ dimensions for each pair of source and sink times, t' and t. As shown in Ref. [16], $N_{\mathrm{eig}} = 32$ provides smearing comparable to that based on Gaussian smearing for $16^3 \times 128$ lattices. We use $N_{\mathrm{eig}} = 32$ in this work. The perambulator matrices provide the quark propagation from all eigenvectors of the Laplacian at the source time to all eigenvectors at the sink time without reference to the operators that are used.

Matrices of correlation functions $C_{ij}(t, t')$ are obtained for four time slices t'. We translate each of these correlation functions to $t' = 0$, yielding $C_{ij}(t, 0)$, and average them for each configuration. The average over gauge configurations of Eq. (8) is calculated using the baryon operators $\Phi_{i,k\ell m}^{\alpha\beta\gamma}(t)$ and $\Phi_{j,\bar{k}\bar{\ell}\bar{m}}^{\bar{\alpha}\bar{\beta}\bar{\gamma}\,\dagger}(0)$ together with perambulators $\tau_{\alpha\bar{\alpha}}^{k\bar{k}}(t, 0)$ for the relevant contractions.

The variational method [17,18] is used to extract the energy levels. We have exploited the fact that the matrices of correlation functions are real-valued within noise after removing a time-independent phase from each operator $B_i(\mathbf{x}, t)$ and the corresponding complex-conjugate phase from $\bar{B}_j(\mathbf{y}, t)$. Imaginary parts of the matrix elements are therefore dropped and that helps to reduce the overall

noise. The Hermitian matrices $C_{ij}(t, 0)$ become real-symmetric matrices.

The generalized eigenvalue problem is solved at time t^* to obtain eigenvectors of the correlation matrices. Because matrix elements of the Hamiltonian involve an average over configurations, we use the correlator matrix averaged over configurations to obtain the eigenvectors as follows,

$$C_{ij}(t^*, 0)u_j^{(n)}(t^*) = \lambda_n(t^*)C_{ij}(t_0, 0)u_j^{(n)}(t^*), \quad (11)$$

where t_0 is the normalization time for which the eigenvalues obey $\lambda_n(t_0) = 1$. Matrix indices i and j each take N_{op} values where N_{op} is the number of operators used. For each gauge configuration, we then calculate matrix elements of $C_{ij}(t, 0)$ in the basis of fixed eigenvectors determined at time t^*, defining the ensemble of effective eigenvalues as follows,

$$\tilde{\lambda}_n(t) = u_i^{(n)\dagger}(t^*)C_{ij}(t, 0)u_j^{(n)}(t^*). \quad (12)$$

At time $t = t^*$, the average over configurations of $\tilde{\lambda}_n(t)$ is equal to $\lambda_n(t)$ because the average correlator matrix was used in Eq. (11). At time $t = t_0$ both the average $\tilde{\lambda}_n(t)$ and $\lambda_n(t)$ equal one for the same reason. The use of fixed eigenvectors provides a smooth time dependence in the diagonal correlation functions, $\tilde{\lambda}_n(t)$, and is consistent with the fact that the eigenvectors of the Hamiltonian should be independent of time. Differences between the fixed and exact eigenvectors contribute at second order to the difference between $\tilde{\lambda}_n(t)$ and $\lambda_n(t)$ owing to the variational nature of the calculation. The accuracy of the fixed eigenvalues analysis has been checked by comparing with the exact eigenvalues. The two analyses agree within uncertainties.

There are two other reasons for using fixed eigenvectors. One is that the eigenvalue problem generally becomes ill-conditioned at late times owing to the exponential decrease of $\lambda_n(t) \propto e^{-E_n(t-t_0)}$ as t becomes large. The higher energy states tend to zero fastest so the condition number of the $N_{\mathrm{op}} \times N_{\mathrm{op}}$ matrix increases exponentially $\propto e^{(E_{\mathrm{high}}-E_{\mathrm{low}})(t-t_0)}$, where E_{high} and E_{low} are the largest and smallest energies obtained from N_{op} operators. For the $N_{\mathrm{op}} = 7$ to 11 operators used, the condition number becomes very large by $t \approx 15$. Backward propagating baryon states can become significant also at large times. When that happens the smallest eigenvalue can pass through zero and become negative. The use of eigenvectors fixed at a time t^* significantly earlier that $t \approx 15$ avoids the conditioning problem.

The second reason for using fixed eigenvectors is that at early times the eigenvectors generally are contaminated by contributions from states above the energy range that is determined by N_{op} operators. By choosing time t_0 to be as large as possible, one reduces the contamination from higher states in the spectrum, which are suppressed by

factors involving e^{-Et_0} as shown in Ref. [19]. We usually set $t^* = t_0 + 1$ in order to diagonalize a matrix that is effectively $e^{-H} \approx 1 - H + \cdots$, with eigenvectors dominated by the Hamiltonian, H. Moreover, a long fitting interval (t_i, t_f) is required for accurate determination of the energies. We balance the requirements by choosing t_0 to be large while keeping t^* small enough to allow a well-conditioned determination of N_{op} eigenvectors. The effective eigenvalues $\tilde{\lambda}_n(t)$ are then fit as described in the next section in order to extract energies.

III. ANALYSIS OF NUCLEON SPECTRA AT $m_\pi = 392(4)$ MeV

Spectra have been calculated for the isospin $\frac{1}{2}$ (N) states, isospin $\frac{3}{2}$ (Δ) states and strangeness -3 (Ω) states using lattices with the three sets of quark masses shown in Table II. In this section we present a detailed discussion of our analysis for the N^* states at the lightest pion mass to show the procedure we employ and to illustrate the quality of the data; the procedure for other cases is similar.

Table V shows the results of fitting each nucleon diagonal correlation function, $\tilde{\lambda}_n(t)$, by a two-exponential function of time as follows,

$$\lambda_{\text{fit}}(t) = (1 - A)e^{-E(t-t_0)} + Ae^{-E'(t-t_0)}, \quad (13)$$

where $E < E'$ so that E is the energy of interest at large time. The second exponential term serves to model the contaminations arising from higher-energy states at early times. The fit window (t_i, t_f) is chosen such that coefficient A is small. The values of t_i and t_f used are given in Table V as are the values of t_0 and diagonalization time t^*. Although the lowest five energies are shown, the number of operators used is 7 to 11 in each irrep as shown in Table IV. Fits are performed for a jackknife ensemble of diagonal correlation functions calculated as in Eq. (12), producing a jackknife ensemble of fit energies whose mean and standard deviation are given in the table.

Plots of the nucleon effective energies, calculated as

$$E_{\text{eff}}(t) = \frac{1}{2} \ln\left(\frac{\tilde{\lambda}(t-1)}{\tilde{\lambda}(t+1)}\right), \quad (14)$$

are shown in Fig. 1 for the G_{1g} and G_{1u} irreps, Fig. 2 for the H_g and H_u irreps, and Fig. 3 for the G_{2g} and G_{2u} irreps. These plots show the values of E_{eff} obtained from Eq. (14) as vertical bars and E_{eff} calculated using the fit function of Eq. (13) in place of $\tilde{\lambda}(t)$ in Eq. (14) as dashed lines. Comparison of the dashed lines with the bars from the lattice ensembles shows the usefulness of two-exponential fits. The term $Ae^{-E'(t-t_0)}$ models the contributions of higher energy states at early times allowing the exponential term $(1 - A)e^{-E(t-t_0)}$ to be determined over a larger fit window (t_i, t_f) than would be possible using a single exponential.

TABLE V. Fit parameters for nucleon states at $m_\pi = 392(4)$ MeV.

IR	(t_0, t^*)	(t_i, t_f)	E	$1 - A$	E'	$\frac{\chi^2}{\text{dof}}$
G_{1g}	(7,8)	(7,31)	0.2085(19)	0.868(26)	0.427(42)	1.63
G_{1g}	(7,8)	(7,24)	0.3545(51)	0.625(31)	0.559(14)	0.49
G_{1g}	(7,8)	(5,22)	0.3675(110)	0.757(63)	0.685(44)	0.66
G_{1g}	(7,8)	(5,18)	0.3831(95)	0.715(44)	0.725(28)	1.02
G_{1g}	(7,8)	(4,15)	0.4205(88)	0.820(35)	0.817(34)	1.39
G_{1g}	(7,8)	(4,14)	0.5320(124)	0.886(32)	0.991(51)	0.83
IR	(t_0, t^*)	(t_i, t_f)	E	$1 - A$	E'	$\frac{\chi^2}{\text{dof}}$
G_{1u}	(7,9)	(6,25)	0.2957(30)	0.840(24)	0.576(28)	0.58
G_{1u}	(7,9)	(5,25)	0.3177(41)	0.895(22)	0.672(40)	1.77
G_{1u}	(7,9)	(4,14)	0.4317(164)	0.758(59)	0.808(39)	0.68
G_{1u}	(7,9)	(4,15)	0.4593(382)	0.720(135)	0.821(72)	1.41
G_{1u}	(7,9)	(4,17)	0.4605(50)	0.914(16)	0.917(36)	1.09
G_{1u}	(7,9)	(4,15)	0.4720(99)	0.806(34)	0.883(30)	0.70
IR	(t_0, t^*)	(t_i, t_f)	E	$1 - A$	E'	$\frac{\chi^2}{\text{dof}}$
H_g	(8,9)	(7,25)	0.3541(54)	0.650(46)	0.547(17)	0.89
H_g	(8,9)	(7,25)	0.3643(29)	0.840(12)	0.633(12)	1.37
H_g	(8,9)	(7,20)	0.3735(93)	0.760(82)	0.610(52)	0.62
H_g	(8,9)	(5,17)	0.4053(56)	0.874(29)	0.740(36)	0.53
H_g	(8,9)	(5,17)	0.4092(64)	0.898(35)	0.753(54)	0.37
H_g	(8,9)	(5,17)	0.4129(77)	0.886(35)	0.808(54)	0.92
IR	(t_0, t^*)	(t_i, t_f)	E	$1 - A$	E'	$\frac{\chi^2}{\text{dof}}$
H_u	(8,9)	(7,25)	0.3037(34)	0.738(38)	0.485(18)	1.08
H_u	(8,9)	(7,25)	0.3065(44)	0.724(50)	0.481(21)	0.72
H_u	(8,9)	(7,24)	0.3203(25)	0.832(22)	0.578(26)	0.84
H_u	(8,9)	(7,24)	0.3383(61)	0.800(61)	0.589(56)	1.04
H_u	(8,9)	(4,18)	0.4516(102)	0.869(31)	0.855(34)	0.63
H_u	(8,9)	(4,18)	0.4628(81)	0.919(24)	0.900(46)	1.35
IR	(t_0, t^*)	(t_i, t_f)	E	$1 - A$	E'	$\frac{\chi^2}{dof}$
G_{2g}	(7,8)	(5,22)	0.3870(69)	0.814(43)	0.737(45)	1.71
G_{2g}	(7,8)	(5,18)	0.3930(85)	0.711(53)	0.675(29)	1.64
G_{2g}	(7,8)	(5,18)	0.4006(80)	0.725(47)	0.704(29)	2.67
G_{2g}	(7,8)	(4,18)	0.4278(73)	0.832(30)	0.852(33)	1.12
G_{2g}	(7,8)	(4,14)	0.5405(205)	0.887(69)	1.000(112)	1.07
G_{2g}	(7,8)	(4,14)	0.5701(129)	0.882(34)	1.032(49)	0.82
IR	(t_0, t^*)	(t_i, t_f)	E	$1 - A$	E'	$\frac{\chi^2}{\text{dof}}$
G_{2u}	(6,8)	(6,23)	0.3407(45)	0.746(42)	0.607(38)	0.70
G_{2u}	(6,8)	(4,15)	0.4586(76)	0.825(28)	0.944(38)	2.41
G_{2u}	(6,8)	(4,16)	0.4802(53)	0.875(23)	0.949(44)	0.69
G_{2u}	(6,8)	(5,16)	0.4958(74)	0.841(26)	0.930(37)	1.60
G_{2u}	(6,8)	(5,16)	0.4992(63)	0.865(19)	1.092(52)	1.23
G_{2u}	(6,8)	(5,15)	0.5239(151)	0.917(56)	1.367(358)	1.96

Fit energy E and uncertainty of the fit energy, σ, are shown by dashed horizontal lines at $E + \sigma$ and $E - \sigma$ extending over the fit window. Note that the fits over a long time interval provide smaller uncertainties when compared with the variations of the effective masses. The latter have contributions from higher states at early times and local fluctuations at late times because they are calculated from the correlation function at next-to-nearest times. Note also that the statistics allow credible determinations of six energy levels in each irrep.
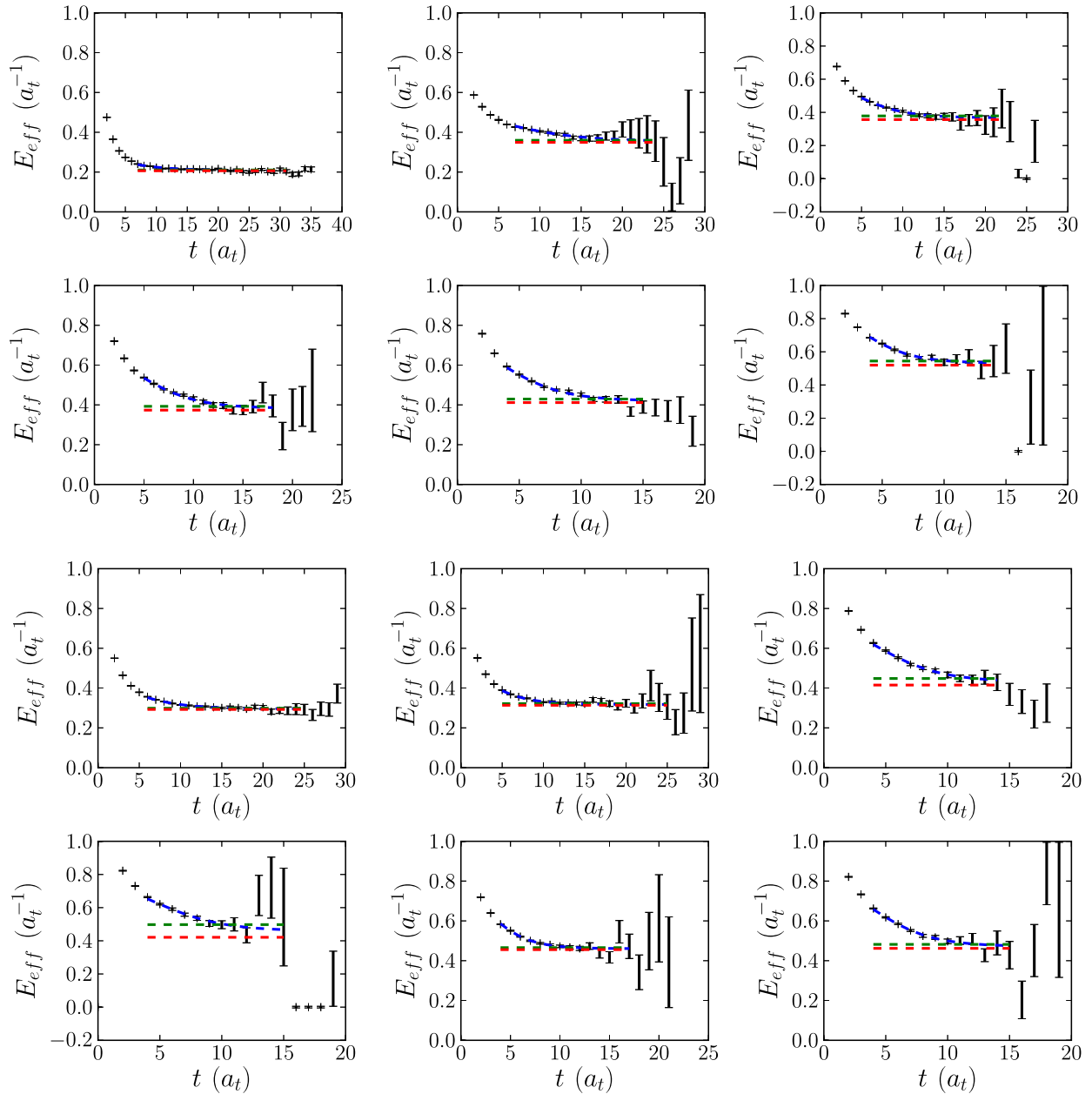
FIG. 1 (color online). Nucleon G_{1g} effective energies are shown for the lowest states in the upper six graphs. The effective energy increases from left to right along the first row and continues to increase from left to right along the second row. The lower six graphs show nucleon G_{1u} effective energies increasing in the same pattern. Calculations are for $m_\pi = 392(4)$ MeV. Vertical bars show the effective energy and the curved dashed line shows the effective energy calculated from the fit function. Horizontal dashed lines show the fit results for $E \pm \sigma$ and their extent shows the fitting interval (t_i, t_f).

The same process has been used to obtain N, Δ, and Ω energies at three values of m_π. The results are given in summary form in the next section.

IV. N, Δ, AND Ω SPECTRA AT THREE PION MASSES

The goal of determining the spectra of baryon resonances from lattice QCD requires an increasing elaborate analysis as the limit of physical pion mass and large volume is approached. Although all lattice states have discrete energies at any finite volume, the energies correspond to single-particle states, interacting multiparticle states and mixtures thereof. At a minimum, one needs to resolve all the states up to some energy and identify them as predominantly resonances or predominantly scattering states. The repulsion or attraction of multiparticle energy levels at finite volume can be related to the momentum-
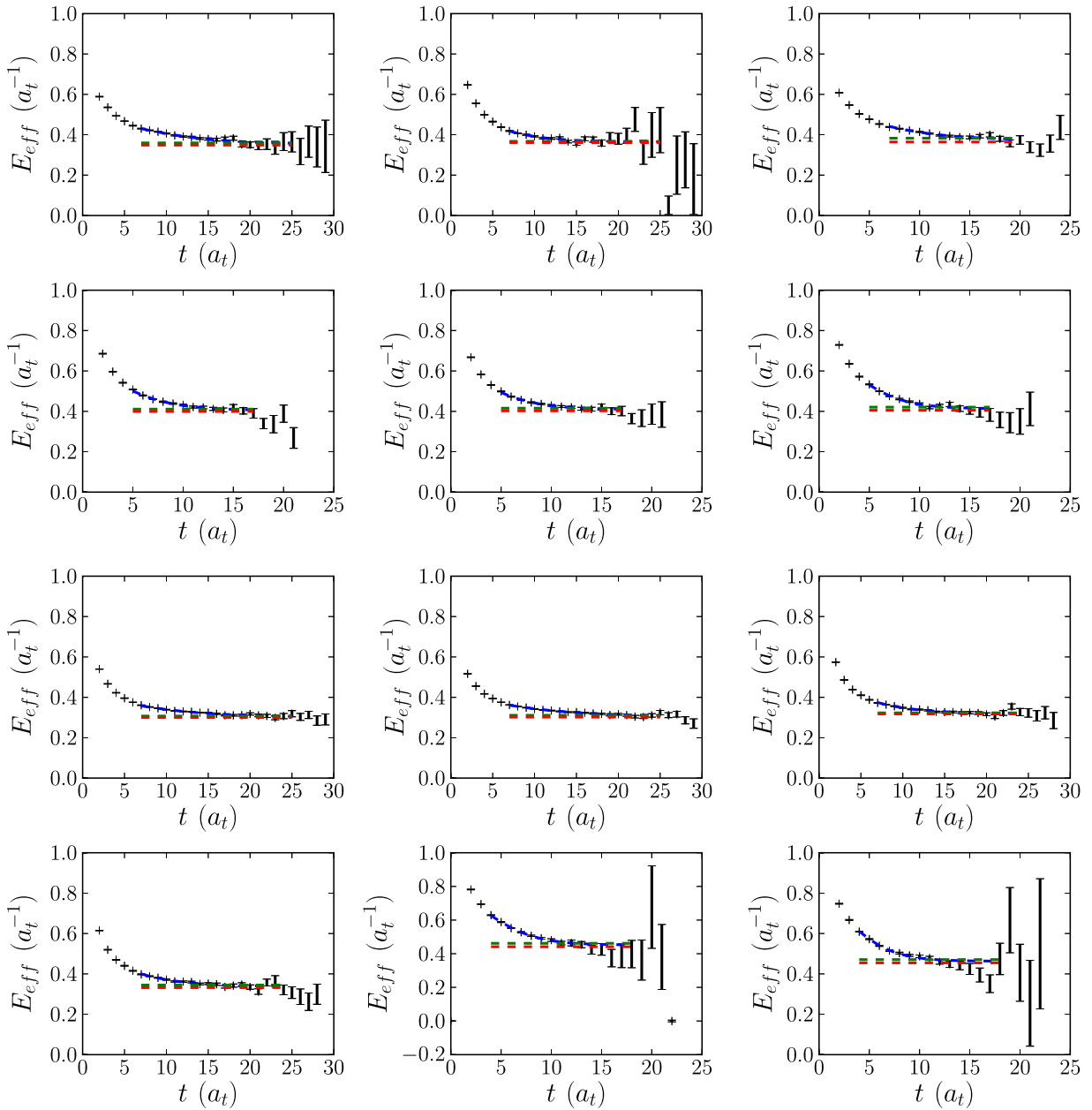
FIG. 2 (color online).   Nucleon H_g effective energies are shown for the lowest states in the upper six graphs and nucleon H_u effective energies are shown in the lower six graphs with effective energies increasing in the same pattern as in Fig. 1. Calculations are for $m_\pi = 392(4)$ MeV. Vertical bars show the effective energy and the curved dashed line shows the effective energy calculated from the fit function. Horizontal dashed lines show the fit results for $E \pm \sigma$ and their extent shows the fitting interval (t_i, t_f).

dependent phase shifts; the (model-dependent) resonance parameters can then be extracted through, say, a Breit-Wigner fit to the phase shift. It also should be noted that experimental resonances generally involve mixtures of single-particle states and multiparticle states and in some cases there may be a linear combination of multiparticle states that produces features similar to those of a resonance.

Although we have spectra for three values of m_π, we cannot clearly delineate multiparticle states in the spectrum and are unable to obtain the energy-dependent phase

shift; that analysis must await the introduction of a broader basis of operators. In the following, we do not attempt to perform a chiral extrapolation on the spectrum. The couplings of the excited states are in general unknown, and we are performing calculations in a region in which, as we will see below, multiparticle contributions are expected.

A. Nucleon spectra

Spectra for isospin $\frac{1}{2}$ states (N states) are summarized in Fig. 4 for each lattice irrep and for $m_\pi = 392, 438,$ and
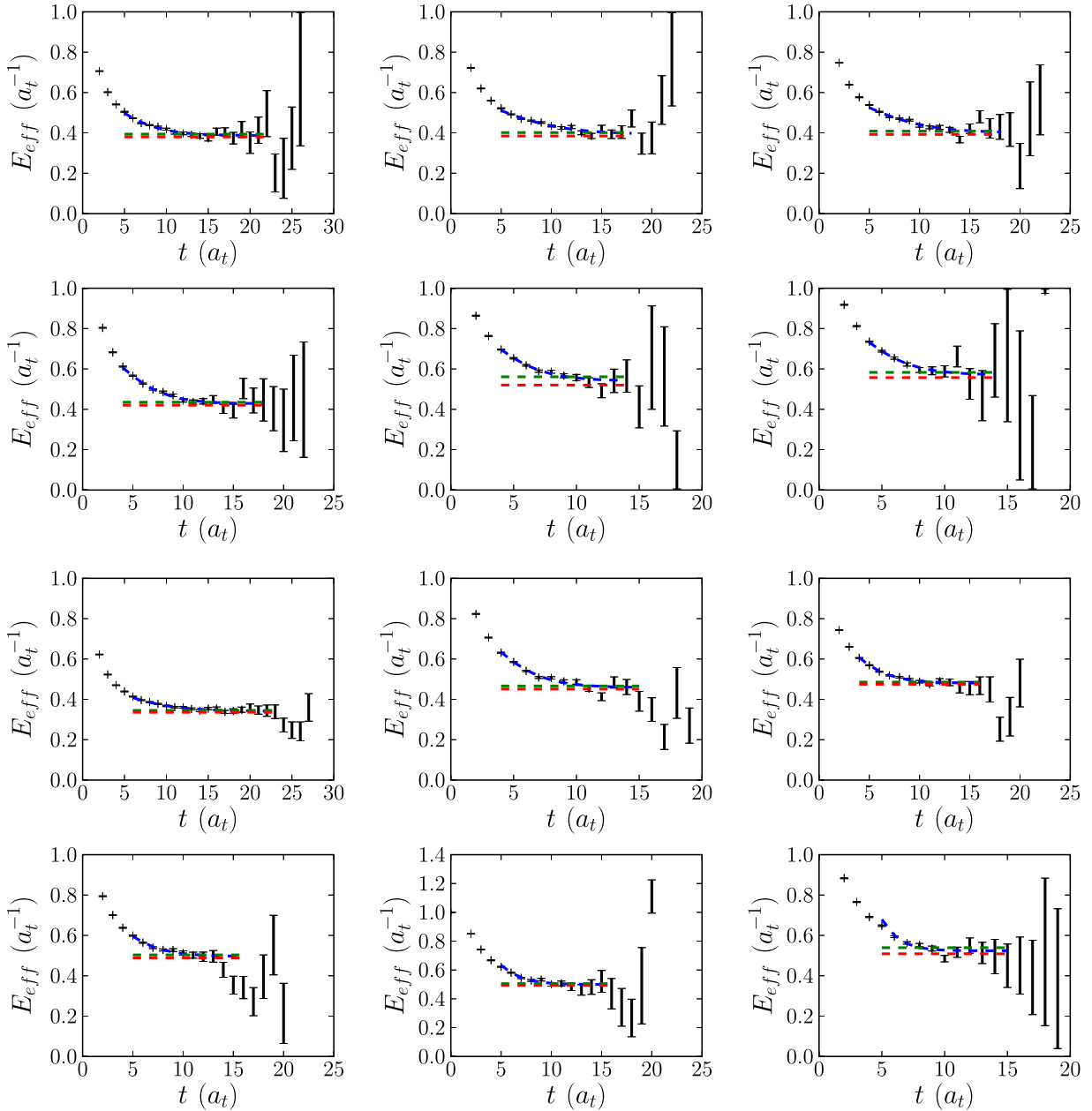
FIG. 3 (color online). Nucleon G_{2g} effective energies are shown for the lowest states in the upper six graphs and nucleon G_{2u} effective energies are shown in the lower six graphs with effective energies increasing in the same pattern as in Fig. 1. Calculations are for $m_\pi = 392(4)$ MeV. Vertical bars show the effective energy and the curved dashed line shows the effective energy calculated from the fit function. Horizontal dashed lines show the fit results for $E \pm \sigma$ and their extent shows the fitting interval (t_i, t_f).

521 MeV. We also show the isospin $\frac{1}{2}$ two-star, three-star and four-star experimental resonances with J^P values that have a subduction to the lattice irrep. Experimental resonances [20] are shown by boxes in columns labeled by their J^P values with the height of the box equal to the full decay width of the resonance. An inner box (color aqua) shows the uncertainty in the Breit-Wigner resonance energy. The lattice results are shown as colored boxes with height equal to 2σ in the columns labeled by values of m_π, where σ is the statistical uncertainty of the fit energy. The lattice

energies have been converted to MeV units by the formula,

$$E = 1672.45 \left(\frac{Ea_t}{m_\Omega a_t} \right)^{\text{latt}}. \tag{15}$$

Here the ratio of a lattice energy and the lattice m_Ω is calculated for each value of m_π and then is scaled by the empirical mass of the Ω-baryon, 1672.45 MeV. Triangles to the right of the lattice spectra for each value of m_π in Fig. 4 point to the threshold for scattering states (multiparticle states) at that value of m_π. Most of the excited
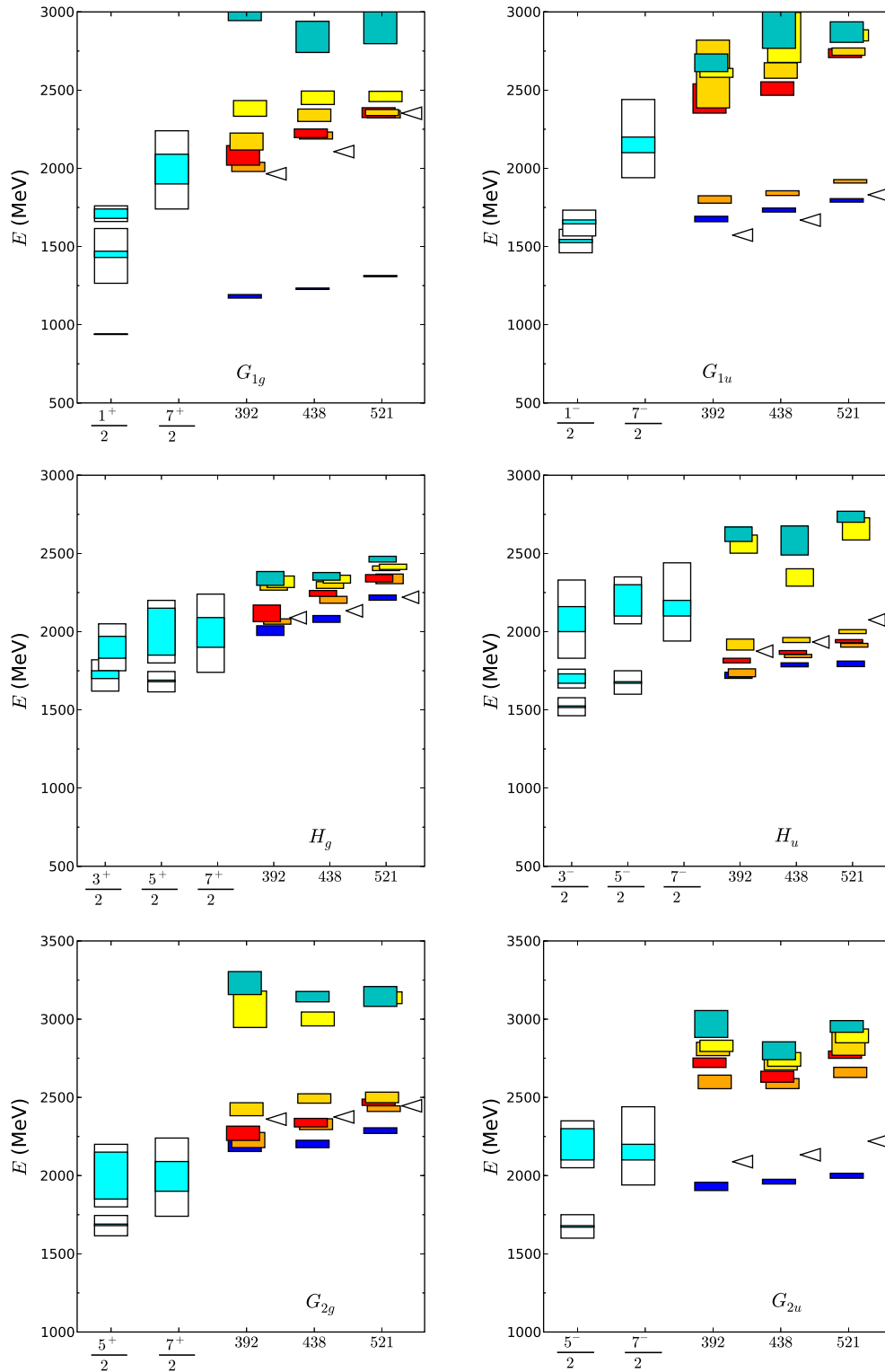
FIG. 4 (color online). Spectra for isospin $\frac{1}{2}$ (nucleon family) at three values of m_π are compared with experimental spectra. Plots in the first row show G_{1g} and G_{1u} lattice irreps, plots in the second row show H_g and H_u irreps and plots in the third row show G_{2g} and G_{2u} irreps. Columns labeled by $m_\pi = 392$, 438, and 521 show lattice spectra at those values of m_π. Two, three and four-star experimental resonances are shown in columns labeled by their J^P values. Each J^P value listed has a subduction to the lattice irrep shown. Each box for an experimental resonance has height equal to the full decay width and an inner box (color aqua) showing the uncertainty in the Breit-Wigner energy. Triangles to the right of lattice spectra point to the threshold for scattering states at that value of m_π.

states have energies higher than the thresholds for scattering states.

As an example, we discuss the G_{1g} plot, shown in the upper left-hand panel of Fig. 4. The experimental spectrum contains three low-lying $\frac{1}{2}^+$ states together with one $\frac{7}{2}^+$ state. For the lattice calculation, we show the six lowest energy states at each pion mass. Each experimental state shown has a subduction to isospin $\frac{1}{2}$, G_{1g}, and should occur in the lattice QCD spectrum for each value of m_π. The lattice states should correspond to subductions of continuum states. The relevant continuum states consist of the experimental resonances and scattering states with J^P values that have subductions to the lattice irrep. Thresholds for scattering states are shown in Fig. 4 and are listed in Table VI. The listed multiparticle states are assigned to lattice irreps following Ref. [21]. Because the spatial lattice is a cube measuring about 1.96 fm on a side, the momentum is restricted to discrete values with the smallest nonzero one being 630 MeV. Consequently, the scattering states with nonzero momenta occur at higher energies.

The general pattern seen in Fig. 4 is that lattice states have high energies that decrease toward the experimental resonances as m_π is decreased. The density of lattice states increases with increasing energy, but we restrict the analysis to the lowest six states. That we are able to extract six energies in each lattice irrep is testament to the effectiveness of the smearing procedure based on eigenvectors of the lattice Laplacian. Note, however, that we cannot distinguish clearly between single- and multiparticle contributions to the spectrum in this calculation.

The nucleon ground state shows up as the lowest state in the G_{1g} lattice irrep. Its energy decreases in a regular manner toward the experimental value shown in the $\frac{1}{2}^+$ column as m_π decreases. The first excited state decreases toward the Roper resonance, $N^*(1440, \frac{1}{2}^+)$ but remains above about 1900 MeV for the pion masses used in this work.

In the negative-parity G_{1u} spectra, there are two low-lying states at each value of m_π and they tend toward the experimental resonances $N(1535, \frac{1}{2}^-)$ and $N(1650, \frac{1}{2}^-)$ as m_π decreases. A number of higher states also tend toward the energy of the $N(2200, \frac{7}{2}^-)$ resonance or to scattering states such $(N\pi)_{s\text{-wave}}$, $(N\pi)_{p\text{-wave}}$ and so on.

Before we discuss the H and G_2 states, it is worth noting that isolated G_2 states do not correspond to any physical state. Because G_2 has minimum spin $\frac{5}{2}$, there must be at least six linearly independent components in the continuum limit. Each G_2 state must have a partner H state with the same parity in order to have an interpretation as a physical state. However, on the lattice discretization effects can cause the H and G_2 partner states to have different energies at $\mathcal{O}(a^2)$.

In the H_g spectra there are five experimental resonances: $N(1720, \frac{3}{2}^+)$ and $N(1900, \frac{3}{2}^+)$, $N(1680, \frac{5}{2}^+)$, $N(2000, \frac{5}{2}^+)$, and $N(1990, \frac{7}{2}^+)$. The lattice states tend as a group toward these energies as m_π decreases.

In the H_u spectra there are four low-lying lattice states near 1800 MeV. The threshold for scattering states is near the same energy as this group of lattice states. Three low-lying experimental resonances are present: N(1530, $\frac{3}{2}^-$), N (1650, $\frac{3}{2}^-$), and N(1675, $\frac{5}{2}^-$).

In our $N_f = 2$ analysis of Ref. [12], we obtained three low-lying H_u states with larger uncertainties. Otherwise the low-lying lattice states agree reasonably well. A test of stability was performed by omitting H_u operators to obtain sets of $N_{op} = 6$, 7, 8, and 9. Spectra were calculated for each of these and the results show three H_u states near 2000 MeV when we use 6 or 7 operators and four H_u states when we use 8 or 9 operators. This behavior suggests that one state is only resolved with the larger number of operators. The operators that are responsible for the appearance of the fourth state are of the triply-displaced-T type. We also have studied the stability of the spectrum at $m_\pi = 561$ MeV by varying t_0, keeping $t^* = t_0 + 1$ and using all

TABLE VI. Multiparticle thresholds on the lattice for isospin I and strangeness S are shown for each value of m_π in MeV. The thresholds are based on the sum of energies of the particles with no interactions.

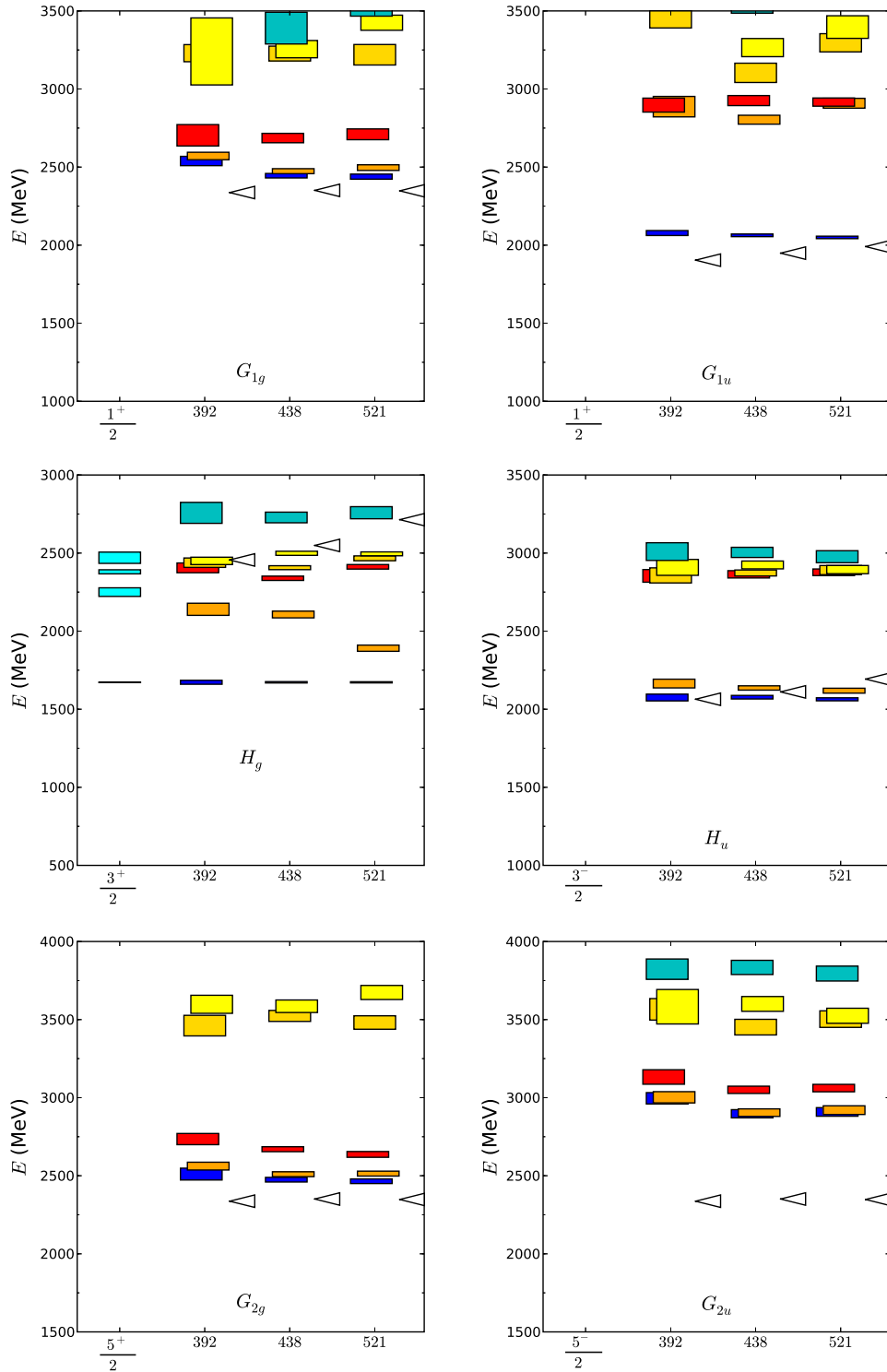| I	S	IR	State	$m_\pi = 392$	$m_\pi = 438$	$m_\pi = 521$
$\frac{1}{2}, \frac{3}{2}$	0	G_{1g}	$(N\pi\pi)_{s\text{-wave}}$	1965(19)	2107(9)	2352(9)
$\frac{1}{2}, \frac{3}{2}$	0	H_g	$(N\pi)_{p\text{-wave}}$	2089(18)	2133(7)	2220(6)
$\frac{1}{2}, \frac{3}{2}$	0	G_{2g}	$(\Delta\pi)_{p\text{-wave}}$	2361(21)	2375(9)	2446(9)
$\frac{1}{2}, \frac{3}{2}$	0	G_{1u}	$(N\pi)_{s\text{-wave}}$	1573(16)	1669(7)	1831(6)
$\frac{1}{2}, \frac{3}{2}$	0	H_u	$(\Delta\pi)_{s\text{-wave}}$	1875(18)	1934(9)	2075(9)
$\frac{1}{2}, \frac{3}{2}$	0	G_{2u}	$(N\pi)_{d\text{-wave}}$	2089(18)	2133(7)	2220(6)
0	−3	G_{1g}	$(\Xi K)_{p\text{-wave}}$	2337(20)	2351(11)	2348(15)
0	−3	H_g	$(\Omega\pi\pi)_{s\text{-wave}}$	2456(20)	2549(9)	2714(9)
0	−3	G_{2g}	$(\Xi K)_{p\text{-wave}}$	2337(20)	2351(11)	2348(15)
0	−3	G_{1u}	$(\Xi K)_{s\text{-wave}}$	1904(18)	1949(12)	1991(17)
0	−3	H_u	$(\Omega\pi)_{s\text{-wave}}$	2064(16)	2111(6)	2193(6)
0	−3	G_{2u}	$(\Xi K)_{d\text{-wave}}$	2337(20)	2351(11)	2348(15)
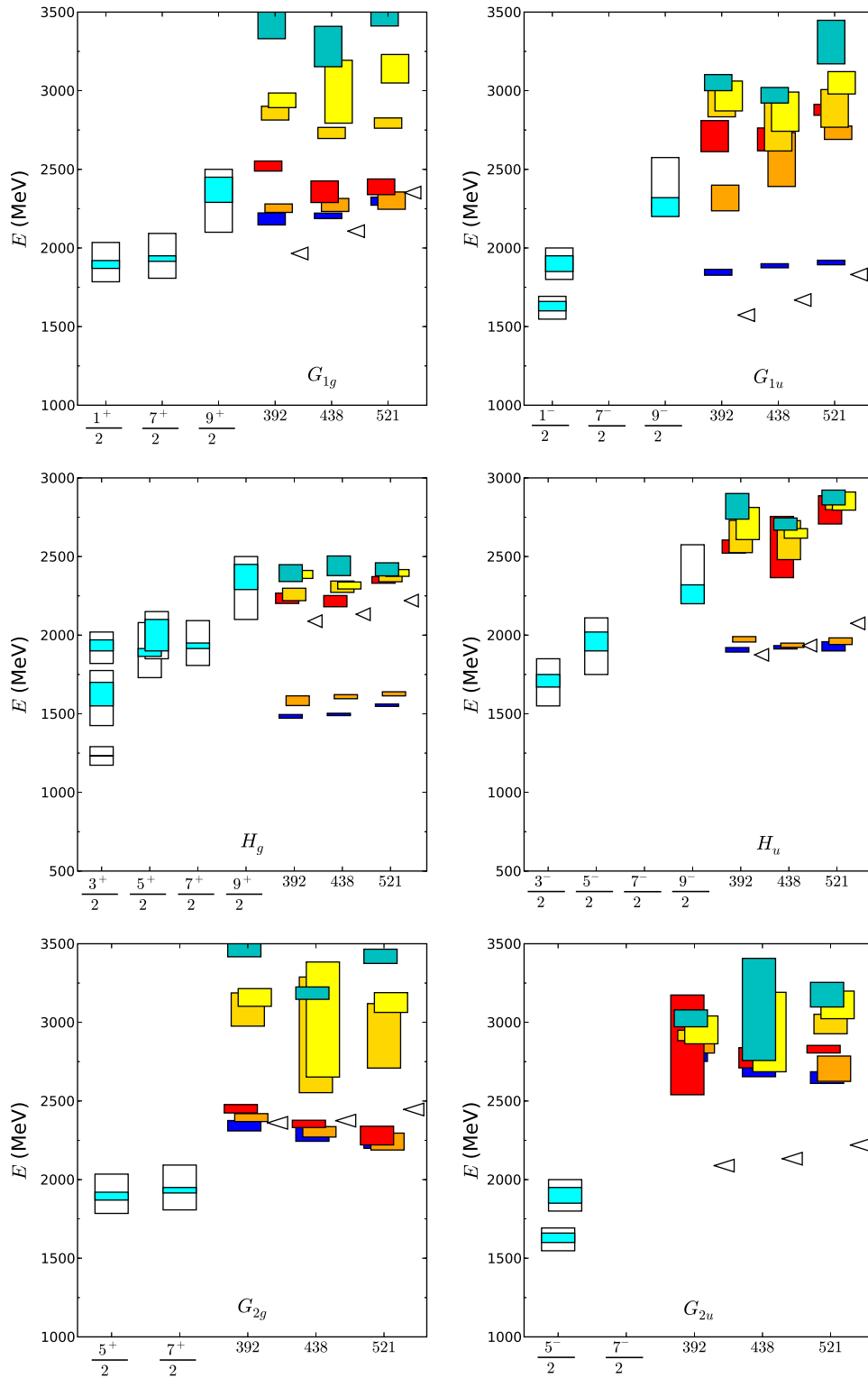
FIG. 5 (color online).   Spectra for isospin $\frac{3}{2}$ (Δ family) at three values of m_π are compared with experimental spectra. Plots in the first row show G_{1g} and G_{1u} lattice irreps, plots in the second row show H_g and H_u irreps and plots in the third row show G_{2g} and G_{2u} irreps. Columns labeled by $m_\pi = 392$, 438, and 521 show lattice spectra at those values of m_π. Two, three and four-star experimental resonances are shown in columns labeled by their J^P values. Each J^P value listed has a subduction to the lattice irrep shown. Each box for an experimental resonance has height equal to the full decay width and an inner box (color aqua) showing the uncertainty in the Breit-Wigner energy. Triangles to the right of lattice spectra point to the threshold for scattering states at that value of m_π.

FIG. 6 (color online).   Spectra for isospin 0, strangeness -3 (Ω family) at three values of m_π are compared with experimental spectra. Plots in the first row show G_{1g} and G_{1u} irreps, plots in the second row show H_g and H_u irreps and plots in the third row show G_{2g} and G_{2u} lattice irreps. Columns labeled by $m_\pi = 392$, 438, and 521 show lattice spectra at those values of m_π. Two, three and four-star experimental resonances are shown in columns labeled by their J^P values. Each J^P value listed has a subduction to the lattice irrep shown. For the Ω, the spins and parities of the experimentally observed states other than the lightest are not clearly determined; for comparison, we assign the states to $\frac{3}{2}^+$, with the heights of the boxes indicating the widths. Triangles to the right of lattice spectra point to the threshold for scattering states at that value of m_π.

operators. For $t_0 = 2, 3, 4, 5, 6, 7,$ and 8 we observe four low-lying states in the nucleon H_u spectrum. The presence of a fourth state is robust when all operators are used.

Four low-lying H_u states are consistent with experiment if one is a scattering state. We have not previously found any evidence for a scattering state with our three-quark operators, but they should be present. Work that is in progress aims to identify the scattering states by using operators designed to couple to them directly.

The pattern that is used to identify a spin $\frac{5}{2}^-$ state on the lattice is a pair of states in the G_{2u} and H_u irreps that become degenerate in the continuum limit. A candidate for this pattern is present in our H_u and G_{2u} spectra: the lowest G_{2u} state and one of the four H_u states at essentially the same energy. The pattern for spin-$\frac{7}{2}$ is a triplet of G_1, H, and G_2 states at essentially the same energy. There are candidates for this pattern in the positive-parity spectra. However, the presence of scattering states makes a secure identification difficult.

B. Δ spectra

The Δ spectra are shown in Fig. 5. The general features are the same as for the nucleon spectra: the lattice states are high and they tend toward the experimental resonances as m_π decreases. The $\Delta(1232, \frac{3}{2}^+)$ ground state appears as the lowest state in the H_g spectra. The next higher H_g state is close to the ground state but appears to tend toward the $\Delta(1600, \frac{3}{2}^+)$ state in the experimental spectrum.

The lowest two G_{1g} states near 2200 MeV appear to be somewhat high but consistent with the experimental resonances $\Delta(1910, \frac{1}{2}^+)$ and $\Delta(1950, \frac{7}{2}^+)$. Candidates for spin-$\frac{7}{2}^+$ partner states are present in the 2200 MeV to 2400 MeV range in H_g and G_{2g} spectra but the pattern is a weak match for the expected degeneracy in the continuum limit. Possibly the small volume used is causing large splittings.

One of the two lowest H_u states corresponds reasonably well to the $\Delta(1700, \frac{3}{2}^-)$ resonance. The other one should correspond to the $\Delta(1930, \frac{5}{2}^-)$ resonance. However, a suitable partner state for spin $\frac{5}{2}^-$ is not seen in the G_{2u} spectrum: the lowest such state is near 2600 MeV. A similar result is found in the G_{2g} spectrum with the lowest state being close to 2300 MeV, well above the energy of the $\Delta(1905, \frac{5}{2}^+)$ resonance. This suggests that the volume may be small, particularly for the G_2 lattice states. In quark models [22,23], excited states typically have larger radii. Our lattice is about 1.8 fm in extent and a state with a radius of more than 1 fm is not expected to be determined well.

C. Ω spectra

The spectra for excited Ω states are shown in Fig. 6. The $\Omega(1672, \frac{3}{2}^+)$ ground state has been used to set the scale for baryon masses so is reproduced perfectly. Experimental resonances above the ground state do not have spin-parity

assignments. In the quality rating of resonances of Ref. [20], $\Omega(2250)$ is rated as a three-star resonance while $\Omega(2380)$ and $\Omega(2470)$ are rated as two-star resonances. The strange-quark mass is at its physical value in our calculations and the dependence on the pion mass is expected to be smaller than for other resonances. Consistent with this the overall pattern of excited states varies little with m_π. A noteworthy exception is the first H_g excited state, whose energy increases from about 1800 MeV to 2100 MeV as the pion mass decreases.

We have considered whether the lattice Ω spectra can provide a useful guide for assignment of spins and parities. We find 11 strangeness −3 states with energies near or below 2500 MeV. Some of those states may be candidates for scattering states rather than resonances. Thresholds for scattering states are shown for each value of m_π in Fig. 6. However we cannot determine whether or not our spectra contain scattering states.

A reasonably good agreement between the lattice and experimental spectra is obtained if the first excited experimental resonance is assigned to $\frac{3}{2}^+$. Beyond that there are several possibilities. In Fig. 6 all of the experimental resonances have been shown in the $\frac{3}{2}^+$ column that appears in the plot of H_g spectra. However, a convincing assignment is not possible because many features of the spectra are not explained. This issue will be revisited when good operators for scattering states are available.

V. SUMMARY

This work represents a milestone in our long-term research program aimed at determining the spectra of baryons in QCD. It provides the first spectrum for N, Δ and Ω baryons based on $N_f = 2 + 1$ QCD with high statistics. A large number of baryon operators is used to calculate matrices of correlation functions. They are analyzed using the variational method with fixed eigenvectors. The analysis provides three spectra at pion masses, $m_\pi = 392(4)$ MeV, 438(3) MeV, and 521(3) MeV.

The lattice volume and pion masses used give considerably higher energies than the experimental resonance energies. However, there is reasonable agreement of the overall pattern of lattice and experimental states. One exception is that almost all G_2 states are much too high. That may be caused by a volume that is too small for highly excited states.

We find candidates for scattering states that have not shown up in our previous analyses based on $N_f = 2$ QCD or quenched QCD. We also find more excited state contamination in the effective-mass plots than was the case for quenched QCD. We expect that when appropriate operators are used to identify multiparticle states, the spectra will be cleaner.

The spectrum of excited states of the Ω baryons has been calculated for the first time. We do not find a close enough agreement between lattice and experimental ex-

cited states to allow a convincing assignment of the unknown spins and parities.

Our main conclusion is that the program to determine baryon spectra from lattice QCD is expected to produce reasonable explanations of the nucleon, Δ and Ω spectra once calculations are extended to smaller pion masses, larger volumes and operators designed to couple to scattering states directly. Stochastic estimation of the quark propagators will allow use of the distillation method with larger volumes [24].

ACKNOWLEDGMENTS

[1] H-W. Lin *et al.* (Hadron Spectrum Collaboration), Phys. Rev. D **79**, 034502 (2009).
[2] S. Durr *et al.*, Science **322**, 1224 (2008).
[3] C. Allton *et al.*, Phys. Rev. D **78**, 114509 (2008).
[4] T. Yamazaki *et al.*, Phys. Rev. D **79**, 114505 (2009).
[5] C. Aubin *et al.*, Nucl. Phys. B, Proc. Suppl. **140**, 231 (2005).
[6] C. Alexandrou *et al.* (ETM Collaboration), Phys. Rev. D **80**, 114503 (2009).
[7] C. Gattringer *et al.* (BGR Collaboration), Phys. Rev. D **79**, 054501 (2009).
[8] A. Bazavov *et al.*, Rev. Mod. Phys. **82**, 1349 (2010).
[9] S. Aoki *et al.* (PACS-CS Collaboration), Phys. Rev. D **81**, 074503 (2010).
[10] S. Basak *et al.*, Phys. Rev. D **76**, 074504 (2007).
[11] T. Burch *et al.*, Phys. Rev. D **74**, 014504 (2006).
[12] J. M. Bulava *et al.* (Hadron Spectrum Collaboration), Phys. Rev. D **79**, 034505 (2009).
[13] I. Aznauryan *et al.*, Phys. Rev. C **80**, 055203 (2009).
[14] R. G. Edwards, B. Joó, and H-W. Lin, Phys. Rev. D **78**, 054501 (2008).

[15] S. Basak *et al.* (Hadron Spectrum Collaboration), Phys. Rev. D **72**, 094506 (2005).
[16] M. Peardon *et al.* (Hadron Spectrum Collaboration), Phys. Rev. D **80**, 054506 (2009).
[17] C. Michael, Nucl. Phys. **B259**, 58 (1985).
[18] M. Lüscher and U. Wolff, Nucl. Phys. **B339**, 222 (1990).
[19] B. Blossier *et al.*, J. High Energy Phys. 04 (2009) 094.
[20] C. Amsler *et al.* (Particle Data Group), Phys. Lett. B **667**, 1 (2008), and 2009 partial update for 2010 edition http://pdg.lbl.gov.
[21] D. C. Moore and G. T. Fleming, Phys. Rev. D **74**, 054504 (2006).
[22] N. Isgur and G. Karl, Phys. Rev. D **19**, 2653 (1979).
[23] S. Capstick and W. Roberts, Prog. Part. Nucl. Phys. **45**, S241 (2000).
[24] C. Morningstar *et al.*, *Hadron 2009: Proceedings of the XIII International Conference on Hadron Spectroscopy*, AIP Conf. Proc. No. 1257, edited by V. Crede, P. Eugenio, and A. Ostrovidov (AIP, New York, 2010), p. 785.
[25] R. G. Edwards and B. Joó (SciDAC Collaboration), Nucl. Phys. B, Proc. Suppl. **140**, 832 (2005).